IEEE Access
Multidisciplinary | Rapid Review | Open Access Journal

Received June 16, 2021, accepted July 4, 2021, date of publication July 7, 2021, date of current version July 13, 2021.

Digital Object Identifier 10.1109/ACCESS.2021.3095407

New Findings on GLRT Radar Detection of Non-Fluctuating Targets via Phased Arrays

FERNANDO DARÍO ALMEIDA GARCÍA[1], MARCO ANTONIO MIGUEL MIRANDA[2], AND JOSÉ CÂNDIDO SILVEIRA SANTOS FILHO[1]

[1]School of Electrical and Computer Engineering, University of Campinas (UNICAMP), Campinas 13083-852, Brazil
[2]Embraer Defesa & Segurança, Campinas 13084-751, Brazil

Corresponding author: Fernando Darío Almeida García (ferdaral@decom.fee.unicamp.br)

This work was supported in part by the Coordenação de Aperfeiçoamento de Pessoal de Nível Superior (CAPES), Brazil, and in part by the Secretaría de Educación Superior, Ciencia, Tecnología e Innovación (SENESCYT), Ecuador.

ABSTRACT This paper addresses the standard *generalized likelihood ratio test* (GLRT) detection problem of weak signals in background noise. In so doing, we consider a non-fluctuating target embedded in complex white Gaussian noise (CWGN), in which the amplitude of the target echo and the noise power are assumed to be unknown. Important works have analyzed the performance for the referred scenario and proposed GLRT-based detectors. Such detectors are projected at an early stage (i.e., prior to the formation of a post-beamforming scalar waveform), thereby imposing high demands on hardware, processing, and data storage. From a hardware perspective, most radar systems fail to meet these strong requirements. In fact, due to hardware and computational constraints, most radars use a combination of analog and digital beamformers (sums) before any estimation or further pre-processing. The rationale behind this study is to derive a GLRT detector that meets the hardware and system requirements. In this work, we design and analyze a more practical and easy-to-implement GLRT detector, which is projected after the analog beamforming. The performance of the proposed detector is analyzed and the probabilities of detection (PD) and false alarm (PFA) are derived in *closed form*. An alternative fast convergent series for the PD is also derived. This series proves to be very efficient and computationally tractable, saving both computation time and computational load. Moreover, we show that in the low signal-to-noise ratio (SNR) regime, the post-beamforming GLRT detector performs better than both the classic pre-beamforming GLRT detector and the square-law detector. This finding suggests that if the signals are weak, instead of processing the signals separately, we first must reinforce the overall signal and then assembling the system's detection statistic. We also showed that the PFA of the post-beamforming GLRT detector is independent of the number of antennas. This property allows us to improve the PD (by increasing the number of antennas) while maintaining a fixed PFA. At last, the SNR losses are quantified, in which the superiority of the post-beamforming GLRT detector was evidenced as the number of antennas and samples increase.

INDEX TERMS *Generalized likelihood ratio test*, non-fluctuating targets, complex white Gaussian noise, phased array radar, probability of detection.

I. INTRODUCTION

Before performing any task (i.e., searching, tracking or imaging), the radar must decide whether the target of interest is present or absent in a certain range, angle or Doppler bin [1]. Unfortunately, the presence of unwanted signals such as thermal noise, clutter, and jamming, ubiquitous in practice, often render this decision very complicated. The optimal decision is achieved by applying the *likelihood ratio test* (LRT) [2]. This decision is based on the Neyman-Pearson (NP) criterion, which maximizes the probability of detection (PD) for a given probability of false alarm (PFA) [3]. The LRT provides an optimal decision if the probability density functions (PDFs) of the received samples are fully known. Of course, this requirement does not fit most practical problems. In view of this, a more general decision rule arose to deal with these types of scenarios, the so-called *generalized likelihood ratio test* (GLRT) [4]. In the GLRT, all unknown PDF parameters

The associate editor coordinating the review of this manuscript and approving it for publication was Guolong Cui.

are replaced by their maximum likelihood estimates (MLEs). This structure allows the GLRT to work over a wide range of scenarios. Although, there is no optimality associated with the GLRT, in practice, it appears to work quite well.

Important GLRT-based detectors were derived considering phased array radars, non-fluctuating targets and, complex white Gaussian noise (CWGN) have been rigorously analyzed in the literature (cf. [5]–[9] for more discussion on this). These works assumed a partial or a complete lack of knowledge about the target and noise statistics. More complex detectors that rely on the use of secondary data can be found in [9]–[16]. In these works, secondary data was assumed to be signal-free from the target components. That is, only noise is present. In particular, the so-called Kelly's detector was derived in [10], which considered that the primary and secondary data vectors share the same unknown noise covariance matrix. In [13], the authors extended the analysis by considering that the target amplitude follows a Gaussian distribution.

All referred works formulate the detection problem at an early stage (i.e., prior to the formation of a post-beamforming scalar waveform), thereby imposing high demands on hardware, processing and data storage. In fact, due to hardware and computational constraints, most radars and mobile applications use a combination of analog and digital beamformers (sums) before any estimation or further pre-processing [17]–[20]. Furthermore, since the use of GLRT involves a high degree of mathematical complexity, theoretical performance analysis can be hampered in most situations. Indeed, this was the case for the aforementioned studies in which their performance metrics – probability of detection (PD) and probability of false alarm (PFA) – were computed through numerical integration, estimated via Monte-Carlo simulations, expressed in integral-form, or require iterative solutions. In this context, we also dedicate our efforts to easy the computation of the performance metrics.

Scanning the technical literature, we realize that no study has been devoted to the development of GLRT radar detectors using a post-beamforming approach. In this paper, we design and evaluate a new GLRT-based detector which is projected after the analog beamforming operation. Moreover, we provide the analytical tools to properly determine the performance of this detector. Specifically, we derive the PD and PFA in *closed form*. An alternative fast convergent series for the PD is also derived. For the analysis, we consider a non-fluctuating target embedded in CWGN, in which the amplitude of the target echo and the noise power are assumed to be unknown. The use of secondary data is not considered. From a mathematical point of view, one could envisage that our detector will somehow provide poorer performance since we are reducing the detection problem dimensionality by means of a sum operation (beamformer). In this paper, we claim that this is not always the case if the signals are weak. In fact, we show that in the low-SNR regime, the post-beamforming GLRT detector performs better than the classic GLRT detector (called here as pre-beamforming GLRT detector [1]) [7, Eq. (6.20)] and then the square-law detector [21, Eq. (15.57)], widely used in non-coherent radars [22]–[24]. This assertion suggest that, instead of processing the signals separately, it is better to adding them up before building the system's detection statistic. Other attractive features about our detector will be discussed throughout this work. With this paper, we aim to take another step towards a better understanding and study of GLRT detectors.

The key contributions of this work may now be summarized as follows:

1) Firstly, we design and evaluate a new GLRT detector projected after the analog beamforming operation. From the practical point of view, this detector meets the hardware and systems requirements of most radar systems.
2) Secondly, we obtain *closed-form* expressions for the corresponding PD and PFA. In particular, the PD is given in terms of the bivariate Fox's H-function, for which we also provide a portable and efficient MATHEMATICA routine.
3) Thirdly, we derive an alternative series representation for the PD, obtained by exploring the orthogonal selection of poles in the Cauchy's residue theorem. This series enjoys a low computational burden and can be quickly executed in any ordinary desktop computer.[2]
4) Finally, we provide some insightful and concluding remarks on the GLRT-based detection for non-fluctuating targets. To do so, we compare the performance of our derived detector with the pre-beamforming GLRT detector.

The remainder of this paper is organized as follows. Section II describes the operation mode of our phased array radar. Section III describes the operation mode of the phased array radar. Section IV characterizes the *detection statistics* and analyzes the corresponding performance metrics. Section V introduces the multivariate Fox's H-function and derives both a *closed-form* solution and a series representation for the PD. Section VI discusses representative numerical results. Finally, Section VII draws the main conclusions.

In what follows, $f_{(\cdot)}(\cdot)$ denotes PDF; $(\cdot)^T$, transposition; $|\cdot|$, modulus; $\mathbf{Re}\,[\cdot]$, real argument; $\mathbf{Im}\,[\cdot]$, imaginary argument; $\|\cdot\|$, Euclidean norm; $\mathbb{E}\,[\cdot]$, expectation; $\mathbb{COV}\,[\cdot]$, covariance; rank$(\cdot)$, rank of a matrix; and $(\cdot)^{-1}$, matrix inversion.

II. RECEIVER'S FRONT–END: PHASED ARRAY

In this work, we consider a linear phased array radar composed of N antennas equally separated in the azimuth direction, as shown in Fig. 1. The transmission and reception processes are carried out as follows. A single antenna transmits a linear frequency-modulated pulse, whereas all

[1] We refer to the detector in [7, Eq. (6.20)] as pre-beamforming GLRT detector since it was conceived and projected over the raw data (i.e., without any pre-processing).

[2] Section VI illustrates the efficiency of this series and compares it with MATHEMATICA's built-in numerical integration.

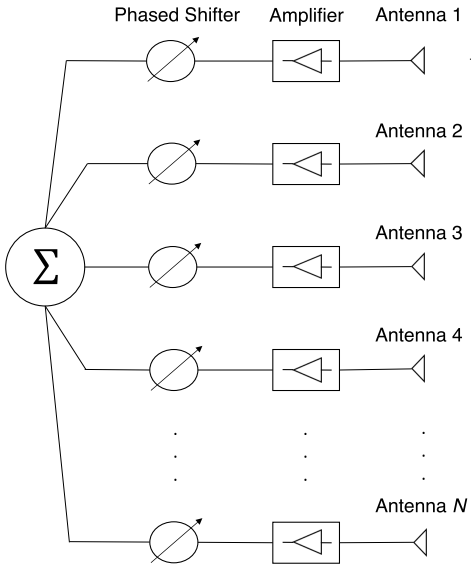

FIGURE 1. Top view of the phased array radar.

antennas receive the echo signals. Furthermore, an amplification block and a phased shifter are installed after each antenna element, and all outputs are added together (i.e., the analog beamforming operation is applied).

Thus, the in-phase and quadrature signals can be written in matrix form, respectively, as

$$X \triangleq \begin{pmatrix} X_{1,1} & X_{2,1} & \cdots & X_{N,1} \\ X_{1,2} & X_{2,2} & \cdots & X_{N,2} \\ \vdots & \vdots & \ddots & \vdots \\ X_{1,M} & X_{2,M} & \cdots & X_{N,M} \end{pmatrix} \tag{1}$$

$$Y \triangleq \begin{pmatrix} Y_{1,1} & Y_{2,1} & \cdots & Y_{N,1} \\ Y_{1,2} & Y_{2,2} & \cdots & Y_{N,2} \\ \vdots & \vdots & \ddots & \vdots \\ Y_{1,M} & Y_{2,M} & \cdots & Y_{N,M} \end{pmatrix}, \tag{2}$$

where $X_{n,m}$ and $Y_{n,m}$ represent the in-phase and quadrature received signals, respectively. In addition, $m \in \{1, 2, \ldots, M\}$ is a discrete-time index, and $n \in \{1, 2, \ldots, N\}$ is a spacial index that denotes the association to the n-th antenna.

For simplicity and without loss of generality, we assume a unity gain and a null phase shift for all antenna elements. In addition, we consider a collection of M signal samples for each of the N antennas. Then, the overall received signal can be written, in vector form, as

$$\underline{R} = [R_1, R_2, \cdots, R_M]^T, \tag{3}$$

where

$$R_m = \sum_{n=1}^{N} \left(X_{n,m} + jY_{n,m}\right). \tag{4}$$

Note that $\underline{R}$ is a complex-valued random vector, in which each component is formed by the sum of the received signals coming from all the antennas at a certain time.

As will be shown in Section III, the fact of adding the target echoes will drastically change the hardware design, detection statistic, and performance of the post-beamforming GLRT detector compared to previous detectors (cf. [7], [9], [10], [12], [13]). Since our detector is projected after the analog beamforming operation, one could argue that its performance would be somehow suboptimum, as compared to the pre-beamforming GLRT detector. In this work, we show that this conclusion not always holds. Indeed, for some cases the post-beamforming GLRT detector overcomes the pre-beamforming GLRT detector. This assertion heavily relies on the SNR of the incoming signals.

III. DETECTION DESIGN VIA POST–BEAMFORMING GLRT

In this section, we present the detection scheme for the post-beamforming GLRT detector.

Herein, the presence or absence of the target is posed over the following *binary hypothesis test*.[3]

A. HYPOTHESIS TEST

- Hypothesis $\mathcal{H}_0$: target is absent. In this case, from the radar model described in the previous section, each $X_{n,m}$ and $Y_{n,m}$ are formed by mutually independent Gaussian components with zero mean and unknown variance σ^2. (Due to the presence of CWGN alone.) Note that σ^2 is the variance for the real ($X_{n,m}$) and imaginary ($Y_{n,m}$) parts individually.
- Hypothesis $\mathcal{H}_1$: target is present. In this case, each $X_{n,m}$ and $Y_{n,m}$ are formed by mutually independent Gaussian components with unknown non-zero means and unknown variance σ^2. (Due to the non-fluctuating target and noise.)

According to the stochastic model described in Section II, the PDF of $\underline{R}$ under $\mathcal{H}_0$ is given by

$$f_{\underline{R}}\left(\underline{r}|\sigma^2; \mathcal{H}_0\right) = \frac{1}{\left(2\pi\sigma^2 N\right)^M} \exp\left[-\frac{\sum_{m=1}^{M} |r_m|^2}{2\sigma^2 N}\right], \tag{5}$$

whereas the PDF of $\underline{R}$ under $\mathcal{H}_1$ is given by (6), displayed at the bottom of the next page, where $\mu_X = \sum_{n=1}^{N} \mu_{X,n}$ and $\mu_Y = \sum_{n=1}^{N} \mu_{Y,n}$ represent the total sum of target echoes for the in-phase and quadrature components, respectively. Note that after the analog beamforming operation, we no longer have access to the specific value of target echo received by a particular antenna, which is what actually occurs in practice.

B. DETECTION RULE

The system's detection statistic can be defined through GLRT as [7]

$$\frac{f_{\underline{R}}\left(\underline{r}|\hat{\sigma}_1^2; \hat{\mu}_X; \hat{\mu}_Y; \mathcal{H}_1\right)}{f_{\underline{R}}\left(\underline{r}|\hat{\sigma}_0^2; \mathcal{H}_0\right)} \underset{\mathcal{H}_0}{\overset{\mathcal{H}_1}{\gtrless}} T, \tag{7}$$

[3] A *binary hypothesis test* refers to the choice that a radar makes between two hypotheses: signal plus interference or only interference. This choice is made throughout all resolution cells [25].

where T is an arbitrary threshold and the ratio on the left-hand side of (7) is called the generalized likelihood ratio. In addition, $\hat{\sigma}_0^2$ is the MLE for σ^2, to be obtained from (5), and $\hat{\sigma}_1^2$, $\hat{\mu}_X$ and $\hat{\mu}_Y$ are the MLEs for σ^2, μ_X and μ_Y, respectively, to be obtained from (6). Eq.(7) implies that the system will decide for $\mathcal{H}_1$ whenever the generalized likelihood ratio exceeds the threshold T, and will decide for $\mathcal{H}_0$ otherwise. Since the logarithmic function is a monotonically increasing function, we can rewrite the GLRT as

$$\ln\left[\frac{f_{\underline{R}}\left(\underline{r}|\hat{\sigma}_1^2;\hat{\mu}_X;\hat{\mu}_Y;\mathcal{H}_1\right)}{f_{\underline{R}}\left(\underline{r}|\hat{\sigma}_0^2;\mathcal{H}_0\right)}\right]\underset{\mathcal{H}_0}{\overset{\mathcal{H}_1}{\gtrless}}\ln\left[T\right]. \tag{8}$$

Note in (5) and (6) that all unknown parameters $\left(\sigma^2, \mu_X \text{ and } \mu_Y\right)$ are scalars quantities. Hence, the corresponding MLEs can be obtained easily. For example, $\hat{\sigma}_0^2$ can be found by taking the natural logarithm of (5), and then taking the derivative with respect to σ^2, i.e.,

$$\frac{\partial \ln\left[f_{\underline{R}}\left(\underline{r}|\sigma^2;\mathcal{H}_0\right)\right]}{\partial\sigma^2} = -\frac{M}{\sigma^2}+\frac{1}{2N\sigma^4}\sum_{m=1}^{M}|r_m|^2. \tag{9}$$

Then, we set (9) equal to zero and solve the equation for σ^2, which yields to

$$\hat{\sigma_0}^2 = \frac{1}{2MN}\sum_{m=1}^{M}|r_m|^2. \tag{10}$$

Using (6) and following the same approach as in (10), the MLEs for μ_X and μ_Y can be calculated, respectively, as

$$\hat{\mu}_X = \frac{1}{M}\sum_{m=1}^{M}\mathbf{Re}\left[r_m\right] \tag{11}$$

$$\hat{\mu}_Y = \frac{1}{M}\sum_{m=1}^{M}\mathbf{Im}\left[r_m\right], \tag{12}$$

whereas the MLE for σ^2 can be computed as follows:

$$\hat{\sigma_1}^2 = \frac{1}{2\,NM}\sum_{m=1}^{M}\left\{\left(\mathbf{Re}\left[r_m\right]-\hat{\mu}_X\right)^2+\left(\mathbf{Im}\left[r_m\right]-\hat{\mu}_Y\right)^2\right\}. \tag{13}$$

(For brevity, we have omitted the derivation steps.)

Substituting (10)–(13) in (8) and after simple simplifications, we have

$$M\ln\left[\left(\frac{\hat{\sigma_0}^2}{\hat{\sigma_1}^2}\right)\right]\underset{\mathcal{H}_0}{\overset{\mathcal{H}_1}{\gtrless}}\ln\left[T\right]. \tag{14}$$

Expanding (13) and after performing some minor manipulations, we can rewrite $\hat{\sigma_1}^2$ as

$$\begin{aligned}\hat{\sigma_1}^2 &= \frac{1}{2\,MN}\sum_{m=1}^{M}\left\{\hat{\mu}_X^2+\hat{\mu}_Y^2\right\}\\ &\quad+\underbrace{\frac{1}{2\,MN}\sum_{m=1}^{M}\left\{\left(\mathbf{Re}\left[r_m\right]\right)^2+\left(\mathbf{Im}\left[r_m\right]\right)^2\right\}}_{\hat{\sigma_0}^2}\\ &\quad+\left(\frac{\hat{\mu}_X}{N}\right)\underbrace{\frac{1}{M}\sum_{m=1}^{M}\mathbf{Re}\left[r_m\right]}_{\hat{\mu}_X}+\left(\frac{\hat{\mu}_Y}{N}\right)\underbrace{\frac{1}{M}\sum_{m=1}^{M}\mathbf{Im}\left[r_m\right]}_{\hat{\mu}_Y}\\ &\overset{(a)}{=}\hat{\sigma_0}^2-\frac{1}{2N}\left(\hat{\mu}_X^2+\hat{\mu}_Y^2\right),\end{aligned} \tag{15}$$

where in step (a) we have used (10), (11), and (12), along with some simplifications.

Isolating $\hat{\sigma}_0^2$ from (15), we obtain

$$\hat{\sigma}_0^2 = \hat{\sigma}_1^2+\frac{1}{2N}\left(\hat{\mu}_X^2+\hat{\mu}_Y^2\right). \tag{16}$$

Replacing (16) in (14), yields

$$M\ln\left[1+\frac{\left(\hat{\mu}_X^2+\hat{\mu}_Y^2\right)}{2\,N\hat{\sigma_1}^2}\right]\underset{\mathcal{H}_0}{\overset{\mathcal{H}_1}{\gtrless}}\ln\left[T\right]. \tag{17}$$

Now, since M and N are a positive numbers, we obtain the same decision as in (17) by simply comparing $\left(\hat{\mu}_X^2+\hat{\mu}_Y^2\right)/\hat{\sigma_1}^2$ with a modified threshold, γ', that is,

$$\frac{\hat{\mu}_X^2+\hat{\mu}_Y^2}{\hat{\sigma_1}^2}\underset{\mathcal{H}_0}{\overset{\mathcal{H}_1}{\gtrless}}\gamma'. \tag{18}$$

For convenience and without loss of generality, we define an equivalent decision rule as[4]

$$Z \triangleq \Psi\frac{\hat{\mu}_X^2+\hat{\mu}_Y^2}{\hat{\sigma_1}^2}\underset{\mathcal{H}_0}{\overset{\mathcal{H}_1}{\gtrless}}\gamma, 6 \tag{19}$$

where Z is the system's detection statistic, $\Psi = (M-1)/2\,N$ is a positive constant, and γ is a new modified threshold.

Fig. 2 illustrates how the pre-beamforming GLRT, the post-beamforming GLRT, and the square-law detectors are constructed. In this figure, $M\,(\cdot)^2$ denotes that M is multiplied by the square of the block input. In particular, Fig. 2-(a) depicts the pre-beamforming GLRT detector architecture. In this case, all received signals are processed separately

[4]The constant Ψ was introduced in the decision rule because it allow us to model Z as a random variable with known PDF, as will become apparent soon.

$$f_{\underline{R}}\left(\underline{r}|\sigma^2;\mu_X;\mu_Y;\mathcal{H}_1\right) = \frac{1}{\left(2\pi\sigma^2\,N\right)^M}\exp\left[-\frac{\sum_{m=1}^{M}\left\{\left(\mathbf{Re}\left[r_m\right]-\mu_X\right)^2+\left(\mathbf{Im}\left[r_m\right]-\mu_Y\right)^2\right\}}{2\sigma^2 N}\right] \tag{6}$$

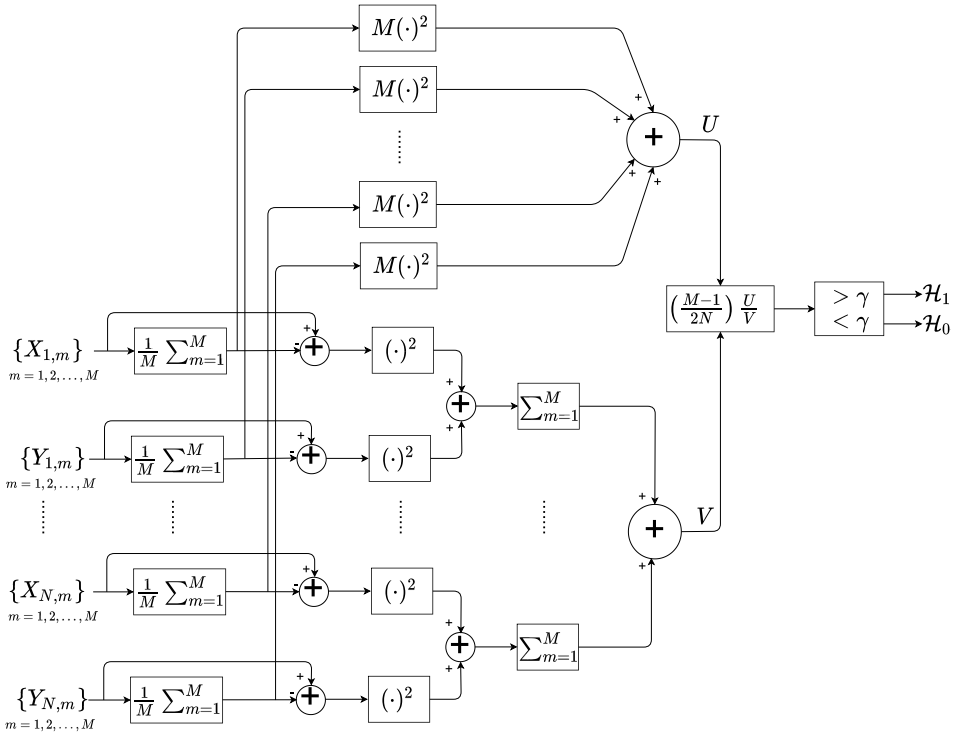

(a) Pre-beamforming GLRT detector [7].

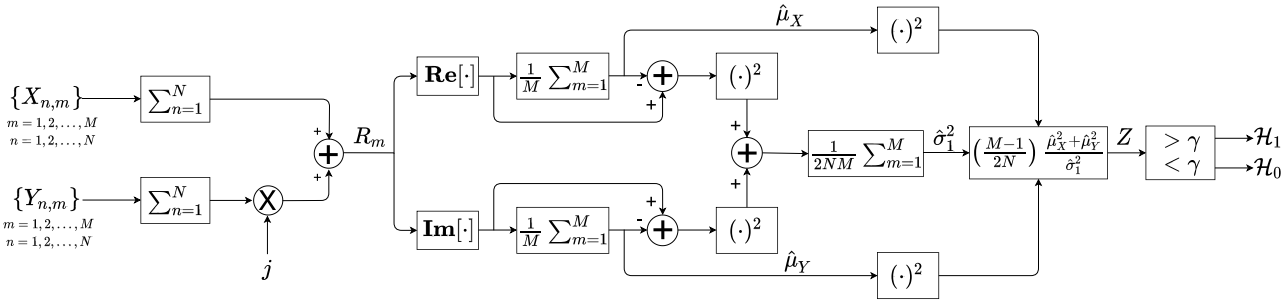

(b) Post-beamforming GLRT detector.

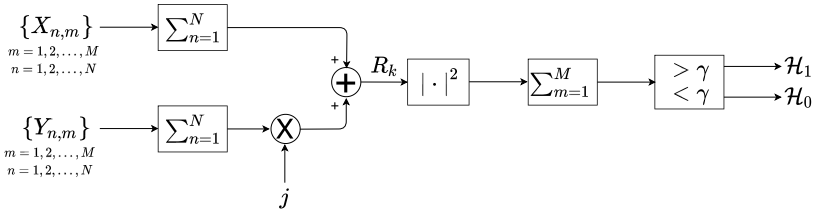

(c) Square-law detector [21].

FIGURE 2. **Detection schemes.**

to form the system's detection statistic [7]. This means that the pre-beamforming GLRT detector requires a dedicated signal-processing chain for each antenna in order to provide the system's detection statistic. That is, the greater the number of antennas, the higher the cost of implementation. Certainly, this type of processing is more difficult to implement due to hardware constraints. Also, a high mathematical complexity of the pre-beamforming GLRT detector arises because all unknown parameters are estimated (via MLE) from a high-dimensional multi-antenna PDF. Fig. 2-(b) illustrates the post-beamforming GLRT detector architecture. Observe that the post-beamforming detector provides a less

restrictive hardware implementation. This is because the beamforming (sum over antennas) operation allows for a single signal-processing chain, while reducing the PDF dimensionality. Finally, Fig. 2-(c) illustrates the square-law detector architecture. Here, after the analog beamforming, the square magnitude of the signal samples is taken and then they are added up together. It is important to emphasize that in order to analytically calculate the performance metrics of the square law detector, we do need the information about the noise power. That is, for a given PFA, the detection threshold is given as a function of the noise power [21].

IV. DETECTION PERFORMANCE

In this section, we characterize and analyze the performance of the post-beamforming GLRT detector. To do so, we start finding the PDFs of Z under $\mathcal{H}_0$ and $\mathcal{H}_1$.

A. DETECTION STATISTICS

First, we rewrite (19) as follows:

$$Z = \frac{(M-1)\left(\hat{\mu}_X^2+\hat{\mu}_Y^2\right)}{2N\hat{\sigma_1}^2} \triangleq \mathcal{I}_1 \overset{(a)}{=} (M-1)\frac{\overbrace{\left(\hat{\mu}_X^2+\hat{\mu}_Y^2\right)M/N\sigma^2}^{\triangleq \mathcal{I}_1}}{\underbrace{2\hat{\sigma_1}^2 M/\sigma^2}_{\triangleq \mathcal{I}_2}}, \tag{20}$$

where in step (a), without affecting the detection performance, we have multiplied the left-hand side of Z by $M\sigma^2/M\sigma^2$.

Note that, to fully characterize Z, it is imperative to find the PDFs of $\mathcal{I}_1$ and $\mathcal{I}_2$ under $\mathcal{H}_0$ and $\mathcal{H}_1$.

Substituting (11) and (12) in $\mathcal{I}_1$, yields to

$$\mathcal{I}_1 = \underbrace{\left(\frac{1}{\sqrt{MN}\sigma}\sum_{k=1}^{M}\mathbf{Re}\left[r_k\right]\right)^2}_{\triangleq U} + \underbrace{\left(\frac{1}{\sqrt{MN}\sigma}\sum_{k=1}^{M}\mathbf{Im}\left[r_k\right]\right)^2}_{\triangleq V}. \tag{21}$$

Observe that U is the square of a Gaussian random variable (RV) with mean $\sqrt{M}\mathbb{E}\left[X_{l,k}\right]/\sigma\sqrt{N}$ and unit variance. In a similar way, V is the square of a Gaussian RV with mean $\sqrt{M}\mathbb{E}\left[Y_{l,k}\right]/\sigma\sqrt{N}$ and unit variance. Therefore, depending on the hypothesis, $\mathcal{I}_1$ can match one of the following conditions:

1) Given $\mathcal{H}_0$: $\mathcal{I}_1$ follows a central chi-squared (CCS) distribution [26] with $\nu_1 = 2$ degrees of freedom.
2) Given $\mathcal{H}_1$: $\mathcal{I}_1$ follows a noncentral chi-squared (NCCS) distribution [27] with noncentral parameter $\lambda_1 = M\left(\mu_X^2+\mu_Y^2\right)/N\sigma^2$ and $\alpha_1 = 2$ degrees of freedom.

Inserting (13) in $\mathcal{I}_2$, we obtain

$$\mathcal{I}_2 = \frac{1}{N\sigma^2}\sum_{m=1}^{M}\left\{\left(\mathbf{Re}\left[r_m\right]-\hat{\mu}_X\right)^2+\left(\mathbf{Im}\left[r_m\right]-\hat{\mu}_Y\right)^2\right\} \tag{22}$$

Here, the analysis is a bit more cumbersome; therefore, we establish the following two lemmas:

Lemma 1: $\mathcal{I}_2$ matches the following conditions:

1) Given $\mathcal{H}_0$: $\mathcal{I}_2$ follows a CCS distribution with $\nu_2 = 2(M-1)$ degrees of freedom.
2) Given $\mathcal{H}_1$: $\mathcal{I}_2$ also follows a CCS distribution with $2(M-1)$ degrees of freedom. In this case, for convenience, we model $\mathcal{I}_2$ by a NCCS distribution with noncentral parameter $\lambda_2 = 0$ and $\alpha_2 = 2(M-1)$ degrees of freedom.

Proof: See Appendix A. ■

Lemma 2: $\mathcal{I}_1$ and $\mathcal{I}_2$ are mutually independent RVs.

Proof: See Appendix B. ■

Then, using Lemmas 1 and 2, we can define $\mathcal{I}_1/\mathcal{I}_2$ as the ratio of either two independent CCS RVs or two independent NCCS RVs, depending on the hypothesis. The factor $(M-1)$ in (20) allows us to model Z by a RV with known PDF.

Given $\mathcal{H}_0$, it can be shown that Z follows a central F-distribution [28] with PDF given by

$$f_Z\left(z|\mathcal{H}_0\right) = \frac{(M-1)^{M-1}(M+z-1)^{-M}}{B(1,M-1)}, \tag{23}$$

where $B(\cdot,\cdot)$ is the Beta function [29, Eq. (5.12.3)]. Using [29, Eq. (5.12.1)], we can rewrite (23) in compact form as

$$f_Z\left(z|\mathcal{H}_0\right) = \left(\frac{M-1}{M+z-1}\right)^M. \tag{24}$$

For the case of $\mathcal{H}_1$, Z can be modeled by a doubly noncentral F-distribution [30], with PDF given by

$$f_Z\left(z|\mathcal{H}_1\right) = \exp\left[-\Upsilon M\right]\left(\frac{M-1}{M+z-1}\right)^M \times {}_1F_1\left(M;1;\frac{\Upsilon z M}{M+z-1}\right), \tag{25}$$

where $\Upsilon = (\mu_X^2+\mu_Y^2)/2N\sigma^2$, and ${}_1F_1(\cdot;\cdot;\cdot)$ is the Kummer confluent hypergeometric function [29, Eq. (13.1.2)]. The equality $\Upsilon = N\ \mathrm{SNR}_n$ holds if $\mathrm{SNR}_n = \mathrm{SNR}_p\ \forall\ (n,p)$, with $\mathrm{SNR}_n = \left(\mu_{X,n}^2+\mu_{Y,n}^2\right)/2\sigma^2$ being the signal-to-noise ratio present at the n-th antenna. The derivation of (25) is shown in Appendix C.

B. FALSE ALARM AND DETECTION PROBABILITIES

It is well known that the performance of any radar system is governed by the PFA and PD. These probabilities can be computed, respectively, as [25]

$$P_{\mathrm{FA}} \triangleq \int_{\gamma}^{\infty} f_Z\left(z|\mathcal{H}_0\right)\,\mathrm{d}z \tag{26}$$

$$P_{\mathrm{D}} \triangleq \int_{\gamma}^{\infty} f_Z\left(z|\mathcal{H}_1\right)\,\mathrm{d}z. \tag{27}$$

Replacing (24) in (26), yields

$$P_{\rm FA} = \left(\frac{M-1}{\gamma+M-1}\right)^{M-1}. \tag{28}$$

Now, isolating γ from (28) we can find a threshold so as to meet a desired PFA, i.e.,

$$\gamma = 1 - M + (M-1)\, {P_{\rm FA}}^{1/(1-M)}. \tag{29}$$

It can be noticed in (29) that we do not need the knowledge of the noise power nor the number of antennas to set the detection threshold. That is, the detection threshold γ is independent of both σ^2 and N. This important feature will allow us to maintain a certain PFA for an arbitrary number of antennas. More precisely, with objective of increasing the PD, we can increase N without worrying about the increase in the PFA.

On the other hand, after substituting (25) in (27), the PD can be obtained in single-integral form as

$$P_{\rm D} = \exp\left[-\Upsilon\, M\right] \int_{\gamma}^{\infty} \left(\frac{M-1}{M+z-1}\right)^{M} \times {}_1F_1\left(M;\, 1;\, \frac{\Upsilon\, z\, M}{M+z-1}\right) {\rm d}z. \tag{30}$$

Certainly, (30) can be evaluated by means of numerical integration. Nonetheless, to further facilitate the computation of the PD, we provide alternative, faster, and more tractable solutions. This is attained in the next section.

V. ALTERNATIVE EXPRESSIONS FOR THE PROBABILITY OF DETECTION

In this section, we provide both a closed-form solution and a fast convergent series for the PD. To this end, we make use of complex analysis and a thorough calculus of residues.

A. THE MULTIVARIATE FOX's H-FUNCTION

We first begin introducing the Fox's H-function, as it will be used throughout this section.

The Fox's H-function has been used in a wide variety of recent applications, including mobile communications and radar systems (cf. [31]–[35] for more discussion on this). In [36], the authors considered the most general case of the Fox's H-function for several variables, defined as

$$\mathbf{H}\left[x;\, (\delta, D)\, ;\, (\beta, B)\, ;\, \mathcal{L}_s\right] \triangleq \left(\frac{1}{2\pi j}\right)^{L} \oint_{\mathcal{L}_s} \Theta\left(s\right) x^{-s} {\rm d}s, \tag{31}$$

in which $j = \sqrt{-1}$ is the imaginary unit, $s \triangleq [s_1, \cdots, s_L]$, $x \triangleq [x_1, \cdots, x_L]$, $\beta \triangleq [\beta_1, \cdots, \beta_L]$, and $\delta \triangleq [\delta_1, \cdots, \delta_L]$ denote vectors of complex numbers, and $B \triangleq \left(b_{i,j}\right)_{n\times L}$ and $D \triangleq \left(d_{i,j}\right)_{m\times L}$ are matrices of real numbers. Also, $x^{-s} \triangleq \prod_{i=1}^{L} x_i^{-s_i}$, ${\rm d}s \triangleq \prod_{i=1}^{L} {\rm d}s_i$, $\mathcal{L}_s \triangleq \mathcal{L}_{s,1} \times \cdots \times \mathcal{L}_{s,L}$, $\mathcal{L}_{s,k}$ is an appropriate contour on the complex plane s_k, and

$$\Theta\left(s\right) \triangleq \frac{\prod_{i=1}^{m} \Gamma\left(\delta_i + \sum_{k=1}^{L} d_{i,k} s_k\right)}{\prod_{i=1}^{n} \Gamma\left(\beta_i + \sum_{k=1}^{L} b_{i,k} s_k\right)}, \tag{32}$$

in which $\Gamma(\cdot)$ is the gamma function [37, Eq. (6.1.1)].

B. FOX's H-FUNCTION-BASED REPRESENTATION

Here, we obtain an alternative closed-form solution for (30), expressed in terms of the Fox's H-function.

To do so, we first perform some mathematical manipulations in (30), resulting in

$$P_{\rm D} = \frac{\exp\left[-\Upsilon\, M\right](M-1)^M}{\Gamma(M)} \int_{\gamma}^{\infty} \left(\frac{1}{M+z-1}\right)^{M} \times G_{1,2}^{1,1}\left[\left.\begin{matrix} 1-M \\ 0,\, 0 \end{matrix}\right| -\frac{\Upsilon\, z\, M}{M+z-1}\right] {\rm d}z, \tag{33}$$

where $G_{m,n}^{p,q}\left[\cdot\right]$ is the Meijer's G-function [38, Eq. (8.2.1.1)].

Now, using the contour integral representation of the Meijer's G-function, we can express (33) as follows:

$$P_{\rm D} = \frac{\exp\left[-\Upsilon\, M\right](M-1)^M}{\Gamma(M)} \int_{\gamma}^{\infty} \left(\frac{1}{M+z-1}\right)^{M} \times \left(\frac{1}{2\pi j}\right) \oint_{\mathcal{L}_{s,1}^{**}} \frac{\Gamma(s_1)\Gamma(M-s_1)}{\Gamma(1-s_1)} \times \left(-\frac{\Upsilon\, z\, M}{M+z-1}\right)^{-s_1} {\rm d}s_1\, {\rm d}z, \tag{34}$$

in which $\mathcal{L}_{s,1}^{**}$ is a closed complex contour that separates the poles of the gamma function $\Gamma(s_1)$ from the poles of $\Gamma(M-s_1)$. Since $\int_{\gamma}^{\infty} \left|f_Z\left(z|\mathcal{H}_1\right)\right| {\rm d}z < \infty$, we can interchange the order of integration [39], i.e.,

$$P_{\rm D} = \frac{\exp\left[-\Upsilon\, M\right](M-1)^M}{\Gamma(M)} \left(\frac{1}{2\pi j}\right) \times \oint_{\mathcal{L}_{s,1}^{**}} \frac{\Gamma(s_1)\Gamma(M-s_1)\left(-\Upsilon\, M\right)^{-s_1}}{\Gamma(1-s_1)} \times \int_{\gamma}^{\infty} \left(\frac{1}{M+z-1}\right)^{M} \left(\frac{z}{M+z-1}\right)^{-s_1} {\rm d}z\, {\rm d}s_1. \tag{35}$$

Developing the inner real integral, we obtain

$$P_{\rm D} = \frac{\exp\left[-\Upsilon\, M\right](M-1)^M \Gamma(M-1)}{\Gamma(M)\ \gamma^{M-1}} \left(\frac{1}{2\pi j}\right) \times \oint_{\mathcal{L}_{s,1}^{*}} \frac{\Gamma(s_1)\Gamma(M-s_1)\left(-\Upsilon\, M\right)^{-s_1}}{\Gamma(1-s_1)} \times {}_2\tilde{F}_1\left(M-1, M-s_1; M; \frac{1-M}{\gamma}\right) {\rm d}s_1, \tag{36}$$

where ${}_2\tilde{F}_1(a,b;c;x) = {}_2F_1(a,b;c;x)/\,\Gamma(c)$ is the regularized Gauss hypergeometric function, and ${}_2F_1(\cdot,\cdot;\cdot;\cdot)$ is the Gauss hypergeometric function [29, Eq. (15.1.1)]. Note that we have used a new complex contour, $\mathcal{L}_{s,1}^{*}$. This is because the inner integration changed the integration path in the complex plane. Here, $\mathcal{L}_{s,1}^{*}$ is a closed contour that separates the poles of $\Gamma(s_1)$ from those of $\Gamma(M-s_1)$.

Finally, replacing (29) in (36) and after using the complex integral representation of the regularized Gauss hypergeometric function [40, Eq. (07.24.26.0004.01)], we can express PD in closed form as in (39), shown at the bottom of the next page, where $\mathcal{L}_s = \mathcal{L}_{s_1} \times \mathcal{L}_{s_2}$, and

$$\Phi = \frac{\Omega^{M-1} \exp\left[-\Upsilon\, M\right]}{\Gamma(M-1)} \tag{37}$$

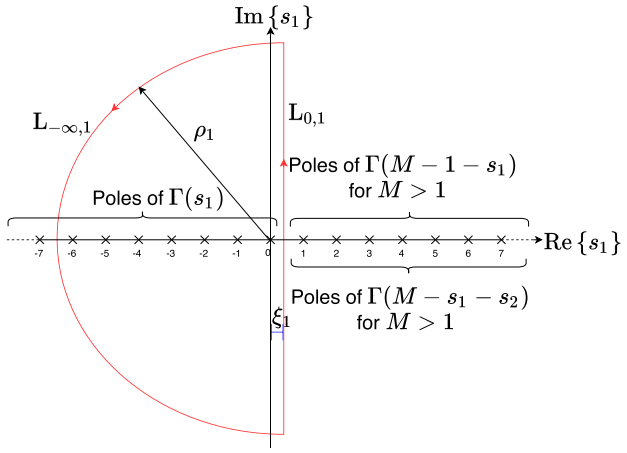

FIGURE 3. Integration path for $\mathcal{L}_{s,1}$.

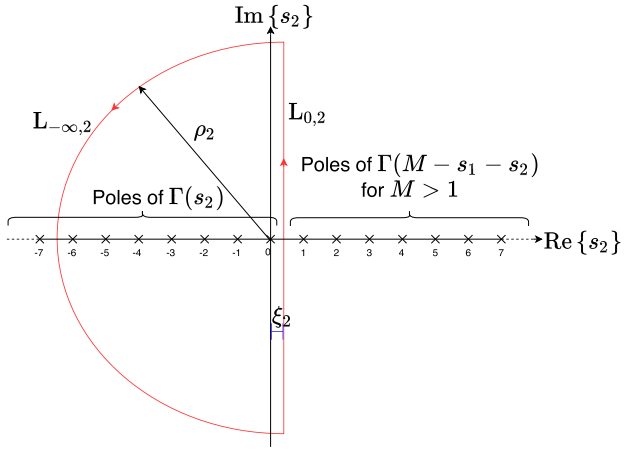

FIGURE 4. Integration path for $\mathcal{L}_{s,2}$.

$$\Omega = \frac{M-1}{1-M+(M-1)\,{P_{\mathrm{FA}}}^{1/(1-M)}}. \tag{38}$$

Observe that (39) has two new closed contours, $\mathcal{L}_{s,1}$ and $\mathcal{L}_{s,2}$. $\mathcal{L}_{s,1}$ is an adjusted contour that appears due to the presence of the new gamma functions, whereas $\mathcal{L}_{s,2}$ is the contour corresponding to the complex representation of the regularized Gauss hypergeometric function. The integration paths for $\mathcal{L}_{s,1}$ and $\mathcal{L}_{s,2}$ are described in Section VI.

A general implementation for the multivariate Fox's H-function is not yet available in mathematical packages such as MATHEMATICA, MATLAB, or MAPLE. Some works have been done to alleviate this problem [41]–[43]. Specifically in [41], the Fox's H-function was implemented from one up to four variables. In this work, we provide an accurate and portable implementation in MATHEMATICA for the bivariate Fox's H-function. The code used to compute (39) is presented in Appendix D. It is important to mention that such implementation is specific for our system model. Moreover, an equivalent series representation for (39) is also provided to facilitate the use of our results. This series representation is presented in the subsequent subsection.

C. INFINITE-SERIES REPRESENTATION

Here, we provide a series representation for (39). To achieve this, we exploit the orthogonal selection of poles in Cauchy's residue theorem.

First, let us consider the following suitable closed contours for (39): (i) $\mathcal{L}_{s,1} = \mathrm{L}_{0,1} + \mathrm{L}_{-\infty,1}$, and (ii) $\mathcal{L}_{s,2} = \mathrm{L}_{0,2} + \mathrm{L}_{-\infty,2}$. Both contours are shown in Figs. 3 and 4, where $\xi_1 \in \mathbb{R}^+$ must be chosen so that all the poles of $\Gamma(s_1)$ are separated from those of $\Gamma(M-1-s_1)$ and $\Gamma(M-s_1-s_2)$, and $\xi_2 \in \mathbb{R}^+$ must be chosen so that all the poles of $\Gamma(s_2)$ are separated from those of $\Gamma(M-s_1-s_2)$. Additionally, ρ_1 and ρ_2 are the radius of the arcs $\mathrm{L}_{-\infty,1}$ and $\mathrm{L}_{-\infty,2}$, respectively.

It is easy to prove that any complex integration along the paths $\mathrm{L}_{-\infty,1}$ and $\mathrm{L}_{-\infty,2}$ will be zero as ρ_1 and ρ_2 go to infinity, respectively. (ρ_1 and ρ_2 tend to infinity since the gamma functions $\Gamma(s_1)$ and $\Gamma(s_2)$ generate simple poles at all non-positive integers [29, Eq. (5.2.1)].) Therefore, the final integration path for $\mathcal{L}_{s,1}$ starts at $\xi_1 - j\infty$ and goes to $\xi_1 + j\infty$, whereas the final integration path for $\mathcal{L}_{s,2}$ starts at $\xi_2 - j\infty$ and goes to $\xi_2 + j\infty$.

Now, we can rewrite (39) through the sum of residues as [44]

$$P_{\mathrm{D}} = \Phi \sum_{k=0}^{\infty}\sum_{l=0}^{\infty} \mathrm{Res}\left[\Xi\left(s_1, s_2\right); s_1 = -k, s_2 = -l\right], \tag{40}$$

where $\mathrm{Res}\left[\Xi\left(s_1, s_2\right); s_1 - k, s_2 = -l\right]$ represents the residue of $\Xi\left(s_1, s_2\right)$ at the poles $s_1 = -k$, $s_2 = -l$, and

$$\Xi\left(s_1, s_2\right) = \frac{\Gamma(s_1)\Gamma(s_2)\Gamma(M-s_1-1)\Gamma(-s_1+M-s_2)}{\Gamma(1-s_2)\Gamma(-(s_1-M))} \times \Omega^{-s_1}\left(-\Upsilon\, M\right)^{-s_2}. \tag{41}$$

is the integration kernel of (39).

Accordingly, after applying the residue operation [44, Eq. (16.3.5)], (40) reduces to

$$P_{\mathrm{D}} = \Phi \sum_{k=0}^{\infty}\sum_{l=0}^{\infty} \left\{ \frac{\Gamma(k+M-1)\Gamma(k+l+M)\left(-\Omega\right)^k}{k!\Gamma(l+1)^2\Gamma(k+M)} \times \left(\Upsilon\, M\right)^l \right\}. \tag{42}$$

Finally, with the aid of [29, Eq. (15.2.1)] and after some mathematical manipulations, we obtain

$$P_{\mathrm{D}} = \exp\left[-\Upsilon\, M\right]\Omega^{M-1} \sum_{k=0}^{\infty} \left\{ \frac{\Gamma(k+M)\left(\Upsilon\, M\right)^k}{\Gamma(k+1)^2} \times {}_2\tilde{F}_1\left(M-1, k+M; M; -\Omega\right) \right\}. \tag{43}$$

$$P_{\mathrm{D}} = \Phi\, \mathbf{H}\left[\left[\Omega, -\Upsilon\, M\right]; \left(\left[0, 0, M-1, M\right], \begin{pmatrix} 1 & 0 & -1 & -1 \\ 0 & 1 & 0 & -1 \end{pmatrix}^T\right); \left(\left[M, 1\right], \begin{pmatrix} -1 & 0 \\ 0 & -1 \end{pmatrix}\right); \mathcal{L}_s\right] \tag{39}$$

It is worth mentioning that (43) is also an original contribution of this work, proving to be very efficient and computationally tractable, as will be shown in the next section.

Generally, when radar designers need to compute the PD over a certain volume (i.e., range, azimuth and elevation), the calculation of the PD has to be performed for all the point scatterers within the entire coverage volume, thus increasing the computational load and simulation time. Eq. (43) can be executed quickly on an ordinary desktop computer, serving as a useful tool for radar designers.

Moreover, if $\mathcal{T}_0 - 1$ terms are used in (43), we can define the truncation error as

$$\mathcal{T} = \frac{1}{\Gamma(M)} \sum_{k=T_0}^{\infty} \frac{\Omega^{M-1} \exp\left[-M\Upsilon\right](M\Upsilon)^k}{\Gamma(k+1)^2} \times \Gamma(k+M)\, {}_2F_1(M-1, k+M; M; \Omega). \quad (44)$$

Since the Gauss hypergeometric function in (19) is monotonically decreasing with respect to k, $\mathcal{T}$ can be bounded as

$$\mathcal{T} \leq {}_2F_1\left(M-1, M+T_0; M; \Omega\right) \times \sum_{k=T_0}^{\infty} \frac{\Omega^{M-1} \exp\left[-M\Upsilon\right](M\Upsilon)^k \Gamma(k+M)}{\Gamma(k+1)^2 \Gamma(M)}. \quad (45)$$

Since we add up strictly positive terms, we have

$$\begin{aligned} &\sum_{k=T_0}^{\infty} \frac{\Omega^{M-1} \exp\left[-M\Upsilon\right](M\Upsilon)^k \Gamma(k+M)}{\Gamma(k+1)^2 \Gamma(M)} \\ &\quad \leq \sum_{k=0}^{\infty} \frac{\Omega^{M-1} \exp\left[-M\Upsilon\right](M\Upsilon)^k \Gamma(k+M)}{\Gamma(k+1)^2 \Gamma(M)} \\ &\quad \overset{(a)}{=} \Omega^{M-1} L_{M-1}(-M\Upsilon), \end{aligned} \quad (46)$$

where in step (a), we have used [40, Eq. (05.02.02.0001.01)] and some minor simplifications. Then, from (45) and (46), (44) can be bounded as

$$\mathcal{T} \leq \frac{L_{M-1}(-M\Upsilon)\, {}_2F_1\left(M-1, M+T_0; M; -\Omega\right)}{\Omega^{1-M}}, \quad (47)$$

where $L_{(\cdot)}(\cdot)$ is the Laguerre polynomial [40, Eq. (05.02.02.0001.01)].

VI. NUMERICAL RESULTS AND DISCUSSIONS

In this section, we validate our derived expressions and discuss the representative results. To do so, we make use of the *receiver operating characteristic* (ROC) curves and Monte-Carlo simulations.[5] For comparison purposes, besides the pre-beamforming GLRT and square-law detectors, we also include the (optimum) LRT detector [7] so as to quantify the SNR losses.[6]

Figs. 5 and 6 show the PDF of Z (analytical and simulated) given the hypotheses $\mathcal{H}_0$ and $\mathcal{H}_1$, respectively. The distribution parameters have been selected to show the broad range of shapes that the PDFs can exhibit. Observe the perfect match between Monte-Carlo simulations and our derived expressions [refer to (24) and (25)].

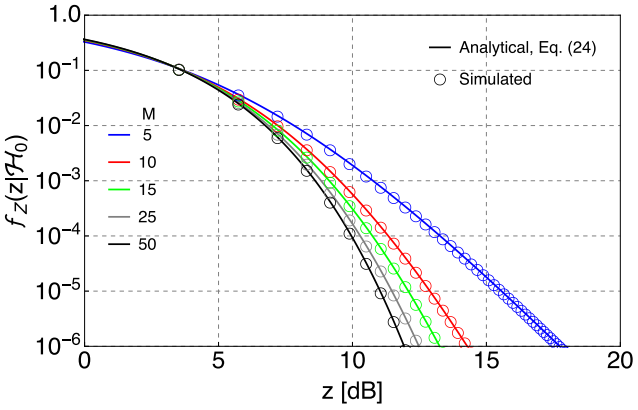

FIGURE 5. PDF of Z under $\mathcal{H}_0$ for different values of M.

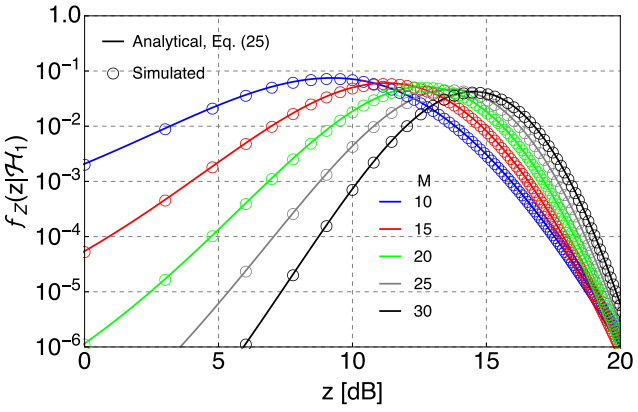

FIGURE 6. PDF of Z under $\mathcal{H}_1$ for different values of M and N.

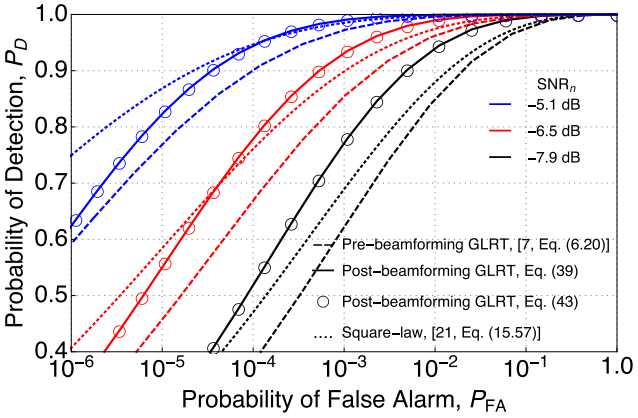

FIGURE 7. P_D vs P_{FA} with $M = 22$, $N = 3$, and different values of SNR$_n$.

Fig. 7 shows P_D as a function of P_{FA} (analytical and simulated) for different values of SNR$_n$. Observe that for low SNR$_n$, the post-beamforming GLRT detector is superior to both the pre-beamforming GLRT detector and the square-law detector. That is, the weaker the signals, the better the performance of our proposed detector. For example,

[5] The number of realizations was set to 1×10^7.

[6] Herein, the SNR loss is defined as extra SNR required to achieved the same performance as the LRT detector [7, Eq. (4.3)], for a given PD.

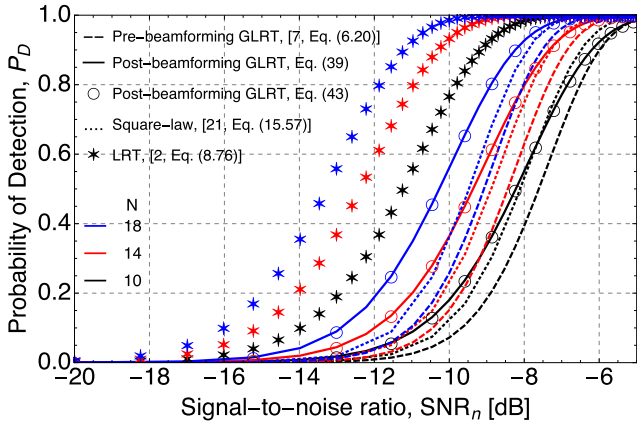

FIGURE 8. P_D vs SNR$_n$ with $M = 15$, $P_{FA} = 10^{-6}$ and different values of N.

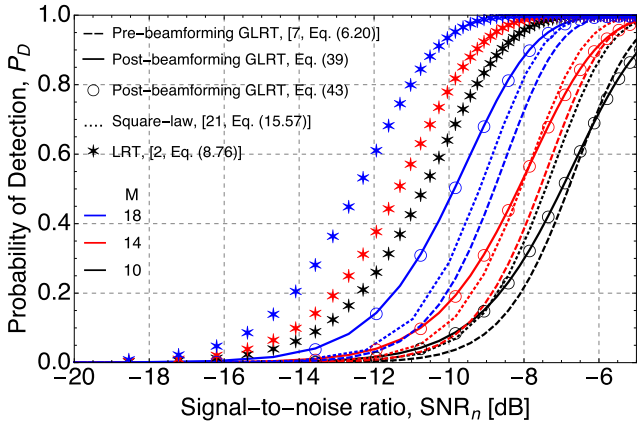

FIGURE 9. P_D vs SNR$_n$ with $N = 11$, $P_{FA} = 10^{-6}$ and different values of M.

given $P_{FA} = 10^{-4}$, the post-beamforming GLRT detector, the pre-beamforming GLRT detector, and the square-law detector provide, respectively, the following probabilities of detection: 0.53, 0.38 and 0.47 for SNR$_n = -7.9$ dB; 0.78, 0.66 and 0.75 for SNR$_n = -6.5$ dB; and finally, 0.94, 0.90 and 0.95 for SNR$_n = -5.1$ dB. The following figures illustrate the impact on the PD as the SNR is reduced.

Fig. 8 shows P_D as a function of SNR$_n$ (analytical and simulated) for different values of N. Note that all detectors improve as the number of antennas increases, requiring a lower SNR for a certain PD. Also, note how the post-beamforming GLRT detector overcomes the pre-beamforming GLRT detector and the square-law detector as the SNR decreases. For example, given SNR$_n = -8$ dB, the post-beamforming GLRT detector, the pre-beamforming GLRT detector, and the square-law detector provide, respectively, the following probabilities of detection: 0.55, 0.40 and 0.54 for $N = 10$; 0.79, 0.64 and 0.75 for $N = 14$; and finally, 0.94, 0.80 and 0.86 for $N = 18$. Additionally, observe how the SNR loss is reduced as N increases. In particular, for a fixed $P_D = 0.8$, the post-beamforming GLRT detector is superior to both the pre-beamforming GLRT detector and the square-law detector deliver, respectively, the following SNR losses: 3.8 dB, 4.2 dB and 2.8 dB for $N = 10$; 2.9 dB, 3.6 dB and 3.1 dB for $N = 14$; and finally, 2.8 dB, 3.9 dB and 3.5 dB for $N = 18$.

Fig. 9 shows P_D as a function of SNR$_n$ (analytical and simulated) for different values of M. Observe that all detectors improve as the number of samples increases. This occurs because we ''average down'' the noise power by increasing M. Once again, the post-beamforming GLRT detector performs better than the pre-beamforming GLRT detector and the square-law detector in the low-SNR regime. More specifically, given SNR$_n = -8$ dB, the post-beamforming GLRT detector, the pre-beamforming GLRT detector and the square-law detector provide, respectively, the following probabilities of detection: 0.30, 0.21 and 0.35 for $M = 10$; 0.53, 0.40 and 0.53 for $M = 14$; and finally, 0.87, 0.73 and 0.82 for $M = 18$. Moreover, observe how the SNR loss is reduced as N increases. In particular, for a fixed $P_D = 0.8$, the post-beamforming GLRT detector, the pre-beamforming GLRT detector and the square-law detector deliver, respectively, the following SNR losses: 3.6 dB, 3.4 dB and 3.2 dB for $M = 10$; 3.4 dB, 3.5 dB and 3.1 dB for $M = 14$; and finally, 2.8 dB, 3.6 dB and 3.1 dB for $M = 18$.

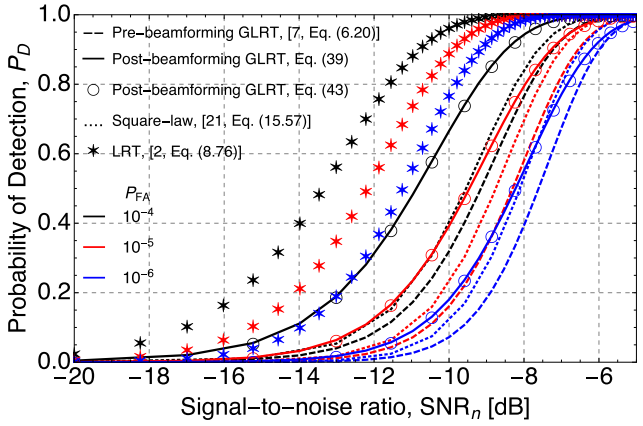

FIGURE 10. P_D vs SNR$_n$ with $M = 10$, $N = 15$ and different values of P_{FA}.

Fig. 10 shows P_D as a function of SNR$_n$ (analytical and simulated) for different values of P_{FA}. Note that all detectors improve as P_{FA} is increased. This fundamental trade-off means that if the PFA is reduced, the PD decreases as well. Observe that for low SNR, the superiority of our detector still remains. For example, given SNR$_n = -8$ dB, the post-beamforming GLRT detector, the pre-beamforming GLRT detector and the square-law detector provide, respectively, the following probabilities of detection: 0.93, 0.76 and 0.84 for $P_{FA} = 10^{-4}$; 0.80, 0.57 and 0.70 for $P_{FA} = 10^{-5}$; and finally, 0.55, 0.40 and 0.54 for $P_{FA} = 10^{-6}$. Additionally, observe how the SNR loss is reduced as N increases. In particular, for a fixed $P_D = 0.8$, the post-beamforming GLRT detector, the pre-beamforming GLRT detector and the square-law detector deliver, respectively, the following SNR losses: 2.4 dB, 3.6 dB and 3.2 dB for $P_{FA} = 10^{-4}$; 2.6 dB, 3.4 dB and 3.0 dB for $P_{FA} = 10^{-5}$; and finally, 2.9 dB, 3.2 dB and 2.8 dB for $P_{FA} = 10^{-6}$.

TABLE 1. Efficiency of (43) as compared to (30).

P_{D} Parameters	P_{D} Value	Absolute Error, ϵ	Number of terms	Computation Time for Eq. (30)	Computation Time for Eq. (43)	Reduction Time
$M = 50$, $P_{FA} = 10^{-8}$, $\Upsilon = -10$ dB	0.106 %	5.471×10^{-10}	23	92.725×10^{-3} (s)	1.923×10^{-3} (s)	97.92 %
$M = 80$, $P_{FA} = 10^{-8}$, $\Upsilon = -10$ dB	1.416 %	5.248×10^{-10}	30	197.044×10^{-3} (s)	2.464×10^{-3} (s)	98.74 %
$M = 100$, $P_{FA} = 10^{-8}$, $\Upsilon = -10$ dB	4.423 %	6.032×10^{-10}	34	294.950×10^{-3} (s)	3.415×10^{-3} (s)	98.84 %
$M = 50$, $P_{FA} = 10^{-8}$, $\Upsilon = -5$ dB	19.224 %	5.261×10^{-10}	45	96.370×10^{-3} (s)	4.625×10^{-3} (s)	95.20 %
$M = 50$, $P_{FA} = 10^{-6}$, $\Upsilon = -5$ dB	52.886 %	5.341×10^{-10}	45	95.769×10^{-3} (s)	4.663×10^{-3} (s)	95.13 %
$M = 50$, $P_{FA} = 10^{-4}$, $\Upsilon = -5$ dB	87.958 %	5.361×10^{-10}	45	92.911×10^{-3} (s)	4.54×10^{-3} (s)	95.11 %
$M = 50$, $P_{FA} = 10^{-6}$, $\Upsilon = -3$ dB	92.089 %	9.339×10^{-10}	60	99.896×10^{-3} (s)	7.043×10^{-3} (s)	92.94 %
$M = 50$, $P_{FA} = 10^{-6}$, $\Upsilon = -2$ dB	98.621 %	4.790×10^{-10}	71	95.124×10^{-3} (s)	9.238×10^{-3} (s)	90.28 %
$M = 50$, $P_{FA} = 10^{-6}$, $\Upsilon = -1$ dB	99.902 %	6.522×10^{-10}	83	98.728×10^{-3} (s)	11.418×10^{-3} (s)	88.43 %

Table 1 illustrates the efficiency of (43) by showing the absolute error, computation time, required number of terms to guarantee a certain accuracy, and reduction time [compared to (30)]. The absolute error can be expressed as

$$\epsilon = |P_{\mathrm{D}} - \overline{P_{\mathrm{D}}}|, \tag{48}$$

where $\overline{P_{\mathrm{D}}}$ is the probability of detection obtained via MATHEMATICA's built-in numerical integration.[7] Observe that for 9 different parameter settings, (43) converges rapidly requiring between 23 and 83 terms to guarantee an accuracy of 10^{-10}. Moreover, the computation time dropped dramatically, thereby providing reduction times above 88%. This impressive reduction can lead to major savings in computational load if one wants to evaluate the detection performance over an entire area or volume covered by the radar system.

VII. CONCLUSION

This paper proposed and analyzed a new GLRT phased array detector, which is projected after the analog beamforming operation. For the analysis, a non-fluctuating target embedded in CWGN was considered. From the practical point of view, this detector fulfills the hardware and computational constraints of most radar systems. The performance metrics – PD and PFA – were derived in *closed form* assuming a total lack of knowledge about the target echo and noise statistics. Moreover, a novel fast convergent series for the PD was also derived. This series representation proved to be very efficient and computationally tractable, showing an outstanding accuracy and impressive reductions in both computational load and computation time, compared to MATHEMATICA's built-in numerical integration. Numerical results showed that when the incoming signals are weak, it is best to combine (sum) them before any estimation or further processing. Indeed, this paper is conclusive in indicating that for low SNR, the post-beamforming GLRT detector shows superior to the pre-beamforming GLRT detector and square-law detectors. Intuitively, this means that if the signal received by each antenna is defectively estimated (due to low target power or strong interference), then the system will also deliver a faulty final estimate. Another interesting feature about the post-beamforming GLRT detector demonstrates that for a fixed PFA, the detection threshold is independent of the number of antennas, which allows us to improve the PD (by increasing N) while maintaining a fixed PFA. The SNR losses were also quantified and they illustrated the superiority of the post-beamforming GLRT detector as N and M increase.

[7] Eq. (30) was evaluated by using the fastest MATHEMATICA's integration method, "`GlobalAdaptive`", with an accuracy goal of 10^{-10}.

APPENDIX A
PROOF OF LEMMA 1

Let us define the following RV

$$\mathcal{I}_3 \triangleq \frac{1}{N\sigma^2}\sum_{m=1}^{M}\left(\mathbf{Re}\left[r_m\right] - \mu_X\right)^2, \tag{49}$$

where μ_X is the total sum of the target echoes for the in-phase components.

Rewriting (49), we have

$$\mathcal{I}_3 = \sum_{m=1}^{M}\left(\frac{\mathbf{Re}\left[r_m\right] - \mu_X}{\sqrt{N}\sigma}\right)^2. \tag{50}$$

It can be noticed that $\mathcal{I}_3$ is a sum of the squares of M standard Gaussian (zero mean and unit variance) RVs. Therefore, $\mathcal{I}_3$ can be modeled by a CCS RV with M degrees of freedom.

Now, after performing some manipulations, we can rewrite (50) as

$$\begin{aligned}
\mathcal{I}_3 &= \sum_{m=1}^{M}\left(\frac{\mathbf{Re}\left[r_m\right] - \hat{\mu}_X}{\sqrt{N}\sigma} + \frac{\hat{\mu}_X - \mu_X}{\sqrt{N}\sigma}\right)^2 \\
&\overset{(a)}{=} \sum_{m=1}^{M}\left(\frac{\mathbf{Re}\left[r_m\right] - \hat{\mu}_X}{\sqrt{N}\sigma}\right)^2 + 2\left(\frac{\hat{\mu}_X - \mu_X}{\sqrt{N}\sigma}\right) \\
&\quad \times \left(\frac{\sum_{m=1}^{M}\mathbf{Re}\left[r_m\right] - M\hat{\mu}_X}{\sqrt{N}\sigma}\right) + \sum_{m=1}^{M}\left(\frac{\hat{\mu}_X - \mu_X}{\sqrt{N}\sigma}\right)^2 \\
&\overset{(b)}{=} \underbrace{\sum_{m=1}^{M}\left(\frac{\mathbf{Re}\left[r_m\right] - \hat{\mu}_X}{\sqrt{N}\sigma}\right)^2}_{\triangleq \mathcal{I}_4} + \underbrace{\left(\frac{\hat{\mu}_X - \mu_X}{\sqrt{N}\sigma/M}\right)^2}_{\triangleq \mathcal{I}_5},
\end{aligned} \tag{51}$$

where in step (b) we use the fact that $M\hat{\mu}_X = \sum_{m=1}^{M}\mathbf{Re}\left[r_m\right]$ and, consequently, the second term in step (a) vanishes. Observe that $\mathcal{I}_5$ represents the square of a standard Gaussian

variable and, therefore, can be modeled by a CCS distribution with one degree of freedom.

Employing the additivity property of the CCS distribution [26] and taking into account the distributions of $\mathcal{I}_3$ and $\mathcal{I}_5$, we can now describe $\mathcal{I}_4$ by a CCS RV with $M-1$ degrees of freedom. Also, observe that $\mathcal{I}_4$ is just the first term of (22).

Following the same approach, it can be prove that the second term in (22) also follows a CCS distribution with $M-1$ degrees of freedom. Since $\mathcal{I}_2$ is formed by the sum of two CCS RVs, then its distribution is governed by a CCS RV with $2(M-1)$ degrees of freedom, which completes the proof. It is worth mentioning that this result remains true regardless of the hypothesis, because any value of μ_X or μ_Y will not affect the distribution of $\mathcal{I}_2$.

APPENDIX B
PROOF OF LEMMA 2

Let

$$P_1 = \mathbf{L}\left(\mathbf{L}^T\mathbf{L}\right)^{-1}\mathbf{L}^T = \frac{1}{M}\mathbf{L}\,\mathbf{L}^T \tag{52}$$

$$P_2 = \mathbf{I} - P_1 = \mathbf{I} - \frac{1}{M}\mathbf{L}\,\mathbf{L}^T \tag{53}$$

be symmetric and idempotent matrices such that rank $(P_1) = \mathbf{L}$, rank $(P_2) = M-1$ and $P_1 + P_2 = \mathbf{I}$, where $\mathbf{I} \in \mathbb{N}^{M\times M}$ represents the identity matrix and $\mathbf{L} = [1, 1, \cdots, 1]^T \in \mathbb{N}^M$ is the unitary vector. In addition, let

$$\mathbf{Re}\left[\underline{r}\right] = \left[\mathbf{Re}\left[r_1\right], \mathbf{Re}\left[r_2\right], \cdots, \mathbf{Re}\left[r_M\right]\right]^T \tag{54}$$

be a random vector with $\mathbb{E}\left[\mathbf{Re}\left[\underline{r}\right]\right] = \mu_X\mathbf{L}$ and $\mathbb{COV}\left[\mathbf{Re}\left[\underline{r}\right]\right] = N\sigma^2\mathbf{I}$. Then, the Cochran's Theorem [45] states that

$$\omega_1 = \frac{\mathbf{Re}\left[\underline{r}\right]^T P_1\,\mathbf{Re}\left[\underline{r}\right]}{N\sigma^2} \tag{55}$$

$$\omega_2 = \frac{\mathbf{Re}\left[\underline{r}\right]^T P_2\,\mathbf{Re}\left[\underline{r}\right]}{N\sigma^2} \tag{56}$$

are independently distributed.

Now, replacing (52) in (55), we have

$$\begin{aligned}\omega_1 &= \frac{1}{N\sigma^2}\mathbf{Re}\left[\underline{r}\right]^T\left(\frac{1}{M}\mathbf{L}\,\mathbf{L}^T\right)\mathbf{Re}\left[\underline{r}\right]\\ &= \frac{1}{MN\sigma^2}\mathbf{Re}\left[\underline{r}\right]^T\mathbf{L}\,\mathbf{L}^T\mathbf{Re}\left[\underline{r}\right]\\ &= \frac{1}{MN\sigma^2}\left(\sum_{k=1}^{M}\mathbf{Re}\left[r_k\right]\right)^2.\end{aligned} \tag{57}$$

Similarly, inserting (53) in (56), we have

$$\begin{aligned}\omega_2 &\overset{(a)}{=} \frac{1}{N\sigma^2}\mathbf{Re}\left[\underline{r}\right]^T P_2^T P_2\mathbf{Re}\left[\underline{r}\right]\\ &= \frac{1}{N\sigma^2}\left\|P_2\mathbf{Re}\left[\underline{r}\right]\right\|^2\\ &\overset{(b)}{=} \frac{1}{N\sigma^2}\left\|\left(\mathbf{I}-\frac{1}{M}\mathbf{L}\,\mathbf{L}^T\right)\mathbf{Re}\left[\underline{r}\right]\right\|^2\\ &\overset{(c)}{=} \frac{1}{N\sigma^2}\left\|\mathbf{Re}\left[\underline{r}\right]-\mathbf{L}\hat{\mu}_X\right\|^2\\ &\overset{(d)}{=} \frac{1}{N\sigma^2}\sum_{k=1}^{M}\left(\mathbf{Re}\left[r_k\right]-\hat{\mu}_X\right)^2,\end{aligned} \tag{58}$$

where in step (a), we have used the definition of idempotent and symmetric matrices [46], in step (b), we have used (53), in step (c), we have employed (11), and in step (d), we have used (54) and applied the Euclidean norm. Observe that ω_1 and ω_2 are the first terms of (21) and (22), respectively. The same approach can also be applied to prove the independence between the second terms. Finally, since $\mathbf{Re}\left[r_k\right]$ and $\mathbf{Im}\left[r_k\right]$ are also independent statistics (cf. Section III-A), then $\mathcal{I}_1$ and $\mathcal{I}_2$ are mutually independent RVs, which completes the proof.

APPENDIX C
DERIVATION OF (25)

To prove (25), we make use of the doubly noncentral F-distribution, defined as [30]

$$\begin{aligned}&f_Z\left(z|\mathcal{H}_1\right)\\ &= \sum_{k=0}^{\infty}\sum_{l=0}^{\infty}\left\{\frac{z^{-1}\exp\left[\frac{-\lambda_1-\lambda_2}{2}\right]\left(\frac{\alpha_1 z}{\alpha_1 z+\alpha_2}\right)^{\frac{\alpha_1}{2}}}{k!\,l!\,B\left(k+\frac{\alpha_1}{2}, l+\frac{\alpha_2}{2}\right)}\right.\\ &\left.\times\left(\frac{\alpha_2}{\alpha_1 z+\alpha_2}\right)^{\frac{\alpha_2}{2}}\left(\frac{\lambda_1\alpha_1 z}{2\left(\alpha_1 z+\alpha_2\right)}\right)^k\left(\frac{\lambda_2\alpha_2}{2\left(\alpha_1 z+\alpha_2\right)}\right)^l\right\}\end{aligned} \tag{59}$$

Rearranging some terms, and after applying [40, Eq. (07.20.02.0001.01)], (59) simplifies to

$$\begin{aligned}f_Z\left(z|\mathcal{H}_1\right) &= z^{-1}\exp\left[\frac{-\lambda_1-\lambda_2}{2}\right]\left(\frac{\alpha_1 z}{\alpha_1 z+\alpha_2}\right)^{\frac{\alpha_1}{2}}\\ &\times\left(\frac{\alpha_2}{\alpha_1 z+\alpha_2}\right)^{\frac{\alpha_2}{2}}\sum_{k=0}^{\infty}\left\{\left(\frac{\lambda_1\alpha_1 z}{2\alpha_1 z+2\alpha_2}\right)^k\right.\\ &\left.\times\frac{{}_1F_1\left(\frac{1}{2}\left(2k+\alpha_1+\alpha_2\right); \frac{\alpha_2}{2}; \frac{\alpha_2\lambda_2}{2(z\alpha_1+\alpha_2)}\right)}{k!\,B\left(k+\frac{\alpha_1}{2}, \frac{\alpha_2}{2}\right)}\right\}.\end{aligned} \tag{60}$$

Now, replacing $\alpha_1 = 2$, $\alpha_2 = 2(M-1)$, $\lambda_1 = M(\mu_X^2 + \mu_Y^2)/N\sigma^2$, and $\lambda_2 = 0$ (cf. Section IV-A) in (60), and after applying [29, Eq. (15.2.1)], and [29, Eq. (5.12.1)], we obtain

$$\begin{aligned}f_Z\left(z|\mathcal{H}_1\right) &= \frac{\exp\left[-\frac{M\left(\mu_X^2+\mu_Y^2\right)}{2N\sigma^2}\right]}{\Gamma(M)}\left(\frac{M-1}{M+z-1}\right)^M\\ &\times\sum_{k=0}^{\infty}\frac{\Gamma(k+M)}{\Gamma(k+1)^2}\left(\frac{Mz\left(\mu_X^2+\mu_Y^2\right)}{2N\sigma^2(M+z-1)}\right)^k.\end{aligned} \tag{61}$$

Finally, after using the definition of the Kummer confluent hypergeometric function [40, Eq. (07.20.02.0001.01)], along

with minor simplifications, we obtain (25), which completes the derivation.

APPENDIX D
MATHEMATICA's IMPLEMENTATION FOR THE BIVARIATE FOX's *H*-FUNCTION

```
ClearAll["Global`*"]; Remove[s];
H[x_, delta_, D_,beta_, B_]
 := Module[{UpP, LoP, Theta,R1, T1, R2, T2, m, n},
 L=Length[Transpose[D]]; (*L represents the
 dimension of the Fox's H-function*)
 m=Length[D]; (*Number of Gamma functions in the
 numerator*)
 n=Length[B]; (*Number of Gamma functions in the
 denominator*)
 S=Table[Subscript[s,i],{i,1,L}]; (*s is the
 vector containing the number of branches, in our
 case s=[s_1,s_2]*)
 UpP=Product[Gamma[delta[[1,j]]+Sum[D[[j,k]]
     S[[k]],{k,1, L}]], {j,1,m}];
 LoP=Product[Gamma[beta[[1,j]]+Sum[B[[j,k]]
     S[[k]],{k,1,L}]],{j,1,n}];
 Theta=UpP/LoP (*Theta computes Eq. (2)*);
 W=50; (*Limit for the complex integration*)
  T=Table[delta[[1,j]]+Sum[D[[j,k]]
  S[[k]],{k,1,L}]>0,{j,1,m}]; (*Generates
  a restriction table*)
 R1=Reduce[And@@Flatten[{T[[1]],T[[3]]}]];
 (*R1 computes the real interval that separates
 the poles of Gamma[s_1] from the poles of
 Gamma[M-1-s_1] and Gamma[M-s_1-s_2]*)
 T1=Mean[{First@R1,Last@R1}];
 R2=Reduce[And@@Flatten[{T[[2]],T[[4]]}]];
 (*R2 computes the real interval that separates
 the poles of Gamma[s_2] from the poles of
 Gamma[M-s_1-s_2]*)
 T2=Mean[{First@R2,Last@R2}];
 W=100; (*Limit for the complex axis*)
 kernel=Theta(x[[1,1]])^(-S[[1]])(x[[1,2]])^(-S[[2]])
   /.{S[[1]]->s1,S[[2]]->s2}; (*Prepare the Kernel
   for Mathematica's Integration*)
 N[1/(2*Pi*I)^2 NIntegrate[kernel,{s1,T1-I W,T1+I W},
 {s2,T2-I W,T2+I W}],20]]
```

REFERENCES

[1] L. V. Blake, *Radar Range-Performance Analysis*, 1st ed. Norwood, MA, USA: Artech House, 1986.
[2] A. Leon-Garcia, *Probability and Random Processes for Electrical Engineering*, 3rd ed. Upper Saddle River, NJ, USA: Prentice-Hall, 1994.
[3] H. Chernoff, "On the distribution of likelihood ratio," *Ann. Math. Statist.*, vol. 25, no. 3, pp. 573–578, Sep. 1954.
[4] S. M. Kay, *Fundamentals of Statistical Signal Processing: Estimation Theory*, 1st ed. Upper Saddle River, NJ, USA: Prentice-Hall, 1993.
[5] S. M. Kendall and A. Stuart, *The Advanced Theory of Statistics*, 2nd ed. New York, NY, USA: Macmillan, 1979.
[6] E. Conte, A. De Maio, and C. Galdi, "Signal detection in compound-Gaussian noise: Neyman-Pearson and CFAR detectors," *IEEE Trans. Signal Process.*, vol. 48, no. 2, pp. 419–428, Feb. 2000.
[7] S. M. Kay, *Fundamentals of Statistical Signal Processing: Detection Theory*, 2nd ed. Upper Saddle River, NJ, USA: Prentice-Hall, 1998.
[8] F. D. A. Garcia, H. R. C. Mora, and N. V. O. Garzon, "GLRT detection of nonfluctuating targets in background noise using phased arrays," in *Proc. Int. Conf. Wireless Mobile Comput., Netw. Commun. (WiMob)*, Barcelona, Spain, Oct. 2019, pp. 1–8.
[9] S. S. Haykin and A. O. Steinhardt, *Adaptive Radar Detection and Estimation*, 1st ed. Hoboken, NJ, USA: Wiley, 1992.
[10] E. J. Kelly, "An adaptive detection algorithm," *IEEE Trans. Aerosp. Electron. Syst.*, vol. AES-22, no. 2, pp. 115–127, Mar. 1986.
[11] I. S. Reed, J. D. Mallett, and L. E. Brennan, "Rapid convergence rate in adaptive arrays," *IEEE Trans. Aerosp. Electron. Syst.*, vol. AES-10, no. 6, pp. 853–863, Nov. 1974.
[12] S. Bose and A. O. Steinhardt, "Optimum array detector for a weak signal in unknown noise," *IEEE Trans. Aerosp. Electron. Syst.*, vol. 32, no. 3, pp. 911–922, Jul. 1996.
[13] O. Besson, A. Coluccia, E. Chaumette, G. Ricci, and F. Vincent, "Generalized likelihood ratio test for detection of Gaussian rank-one signals in Gaussian noise with unknown statistics," *IEEE Trans. Signal Process.*, vol. 65, no. 4, pp. 1082–1092, Feb. 2017.
[14] N. B. Pulsone and C. M. Rader, "Adaptive beamformer orthogonal rejection test," *IEEE Trans. Signal Process.*, vol. 49, no. 3, pp. 521–529, Mar. 2001.
[15] F. C. Robey, D. R. Fuhrmann, E. J. Kelly, and R. Nitzberg, "A CFAR adaptive matched filter detector," *IEEE Trans. Aerosp. Electron. Syst.*, vol. 28, no. 1, pp. 208–216, Jan. 1992.
[16] W. Liu, J. Liu, C. Hao, Y. Gao, and Y.-L. Wang, "Multichannel adaptive signal detection: Basic theory and literature review," 2021, *arXiv:2102.03474*. [Online]. Available: https://arxiv.org/abs/2102.03474
[17] S. Zhang, C. Guo, T. Wang, and W. Zhang, "ON–OFF analog beamforming for massive MIMO," *IEEE Trans. Veh. Technol.*, vol. 67, no. 5, pp. 4113–4123, Jan. 2018.
[18] S. Huber, M. Younis, A. Patyuchenko, G. Krieger, and A. Moreira, "Spaceborne reflector SAR systems with digital beamforming," *IEEE Trans. Aerosp. Electron. Syst.*, vol. 48, no. 4, pp. 3473–3493, Oct. 2012.
[19] S. R. J. Axelsson, "Noise radar for range/Doppler processing and digital beamforming using low-bit ADC," *IEEE Trans. Geosci. Remote Sens.*, vol. 41, no. 12, pp. 2703–2720, Dec. 2003.
[20] D. Zhu, B. Li, and P. Liang, "A novel hybrid beamforming algorithm with unified analog beamforming by subspace construction based on partial CSI for massive MIMO-OFDM systems," *IEEE Trans. Commun.*, vol. 65, no. 2, pp. 594–607, Feb. 2017.
[21] M. A. Richards, J. Scheer, W. A. Holm, and W. L. Melvin, *Principles of Modern Radar: Basic Principles*, 1st ed. West Perth, WA, Australia: SciTech, 2010.
[22] G. V. Weinberg, "Noncoherent radar detection in correlated Pareto distributed clutter," *IEEE Trans. Aerosp. Electron. Syst.*, vol. 53, no. 5, pp. 2628–2636, Oct. 2017.
[23] G. V. Weinberg and C. Tran, "Noncoherent detector threshold determination in correlated Pareto distributed clutter," *IEEE Geosci. Remote Sens. Lett.*, vol. 16, no. 3, pp. 372–376, Mar. 2019.
[24] G. V. Weinberg, "Minimum-based sliding window detectors in correlated Pareto distributed clutter," *IEEE Geosci. Remote Sens. Lett.*, vol. 14, no. 11, pp. 1958–1962, Nov. 2017.
[25] M. I. Skolnik, *Introduction to Radar Systems*, 3rd ed. New York, NY, USA: McGraw-Hill, 2001.
[26] A. Papoulis, *Probability, Random Variables, and Stochastic Processes*, 4th ed. New York, NY, USA: McGraw-Hill, 2002.
[27] P. B. Patnaik, "The non-central χ^2 and F-distributions and their applications," *Biometrika*, vol. 36, no. 1, pp. 202–232, Jun. 1949.
[28] P. C. B. Phillips, "The true characteristic function of the f distribution," *Biometrika*, vol. 69, no. 1, pp. 261–264, 1982.
[29] F. W. J. Olver, D. W. Lozier, R. F. Boisvert, and C. W. Clark, *NIST Handbook of Mathematical Functions*, 1st ed. Washington, DC, USA: US Dept. Commerce, National Institute of Standards and Technology (NIST), 2010.
[30] W. G. Bulgren, "On representations of the doubly non-central F distribution," *J. Amer. Statist.*, vol. 66, no. 333, pp. 184–186, Mar. 1971.
[31] F. D. A. Garcia, A. C. F. Rodriguez, G. Fraidenraich, and J. C. S. S. Filho, "CA-CFAR detection performance in homogeneous Weibull clutter," *IEEE Geosci. Remote Sens. Lett.*, vol. 16, no. 6, pp. 887–891, Jun. 2019.
[32] Y. A. Rahama, M. H. Ismail, and M. S. Hassan, "On the sum of independent fox's H-function variates with applications," *IEEE Trans. Veh. Technol.*, vol. 67, no. 8, pp. 6752–6760, Aug. 2018.
[33] C. R. N. da Silva, E. J. Leonardo, and M. D. Yacoub, "Product of two envelopes taken from $\alpha-\mu$, $\kappa-\mu$ and $\eta-\mu$ distributions," *IEEE Trans. Commun.*, vol. 66, no. 99, pp. 1284–1295, Mar. 2017.
[34] C. H. M. de Lima, H. Alves, and P. H. J. Nardelli, "Fox H-function: A study case on variate modeling of dual-hop relay over Weibull fading channels," in *Proc. IEEE Wireless Commun. Netw. Conf. (WCNC)*, Apr. 2018, pp. 1–5.
[35] F. D. A. García, H. R. C. Mora, N. V. O. Garzón, and J. C. S. S. Filho, "Alternative representations for the probability of detection of non-fluctuating targets," *Electron. Lett.*, vol. 56, no. 21, pp. 1136–1139, Oct. 2020.
[36] N. T. Hai and H. M. Srivastava, "The convergence problem of certain multiple Mellin-Barnes contour integrals representing H-functions in several variables," *Comput. Math. Appl.*, vol. 29, no. 6, pp. 17–25, Mar. 1995.

[37] M. Abramowitz and I. A. Stegun, *Handbook of Mathematical Functions With Formulas, Graphs, and Mathematical Tables*, 10th ed. Washington, DC, USA: US Dept. Commerce, National Bureau of Standards, 1972.
[38] A. P. Prudnikov, Y. A. Bryčkov, and O. I. Maričev, *Integral and Series*, vol. 3, Fizmatlit, Ed., 2nd ed. Moscow, Russia: Fizmatlit, 2003.
[39] G. Fubini, "Sugli integrali multipli," *Rom. Acc. L. Rend.*, vol. 16, no. 1, pp. 608–614, 1907.
[40] Wolfram Research, Inc. (2018). *Wolfram Research*. Accessed: Sep. 19, 2020. [Online]. Available: https://functions.wolfram.com
[41] H. R. Alhennawi, M. M. H. El Ayadi, M. H. Ismail, and H. A. M. Mourad, "Closed-form exact and asymptotic expressions for the symbol error rate and capacity of the H-function fading channel," *IEEE Trans. Veh. Technol.*, vol. 65, no. 4, pp. 1957–1974, Apr. 2016.
[42] F. Yilmaz and M.-S. Alouini, "Product of the powers of generalized Nakagami-m variates and performance of cascaded fading channels," in *Proc. IEEE Global Telecommun. Conf. (GLOBECOM)*, Abu Dhabi, UAE, Nov. 2009, pp. 1–8.
[43] F. D. A. Garcia, H. R. C. Mora, G. Fraidenraich, and J. C. S. S. Filho, "Square-law detection of exponential targets in Weibull-distributed ground clutter," *IEEE Geosci. Remote Sens. Lett.*, early access, Jul. 22, 2020, doi: 10.1109/LGRS.2020.3009304.
[44] E. Kreyszig, *Advanced Engineering Mathematics*, 10th ed. Hoboken, NJ, USA: Wiley, 2010.
[45] W. G. Cochran, "The distribution of quadratic forms in a normal system, with applications to the analysis of covariance," *Math. Proc. Cambridge Phil. Soc.*, vol. 30, no. 2, pp. 178–191, Apr. 1934.
[46] M. D. Springer, *The Algebra of Random Variables*. New York, NY, USA: Wiley, 1979.

FERNANDO DARÍO ALMEIDA GARCÍA received the B.Sc. degree in electrical and telecommunications engineering from Armed Forces University–ESPE, Sangolquí, Ecuador, in 2012, and the M.Sc. degree in electrical engineering from the University of Campinas (UNICAMP), SP, Brazil, in 2015, where he is currently pursuing the Ph.D. degree. Since 2014, he has been working together with Bradar Indústria S.A., a branch of Embraer Defense & Security, in the design and development of novel radar signal processing techniques. His research interests include radar systems and channel modeling.

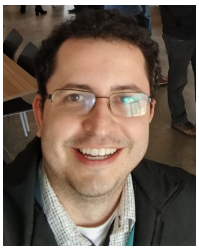

MARCO ANTONIO MIGUEL MIRANDA was born in Brazil, in 1987. He received the B.Sc. and M.Sc. degrees from the University of Campinas (UNICAMP), Campinas, Brazil, in 2010 and 2013, respectively. He is currently pursuing the Ph.D. degree in weather radar technology. Since 2014, he has been working as a Radar Signal Processing Team Leader at Embraer Defense & Security developing radar systems applied to ground and air surveillance and defense.

JOSÉ CÂNDIDO SILVEIRA SANTOS FILHO received the B.Sc., M.Sc., and Ph.D. degrees from the School of Electrical and Computer Engineering (FEEC), University of Campinas (UNICAMP), Campinas, SP, Brazil, in 2001, 2003, and 2006, respectively, all in electrical engineering. From 2006 to 2009, he was a Postdoctoral Fellow with the Wireless Technology Laboratory (WissTek), FEEC, UNICAMP, where he is currently an Associate Professor. Since 2011, he has regularly consulted for Bradar Indústria S.A., a branch of Embraer Defense & Security, to assist in the development of advanced radar techniques and systems. From June 2018 to September 2019, he was a Visiting Researcher with Harvard University. He has published over 100 technical articles, about half of which in international journals. His research interests include wireless communications and radar systems. He was ranked first in his undergraduate program, and his Ph.D. Thesis was awarded an Honorary Mention by the Brazilian Ministry of Education (CAPES), in 2007 CAPES Thesis Contest. He has served as a Reviewer for many prestigious journals and conferences worldwide.